Interface Engineering in Perovskite Solar Cells by low concentration of PEAI solution in the antisolvent step

Teresa S. Ripolles,[1†] Patricio Serafini,[2†] Carlos Redondo-Obispo,[1,3] Esteban Climent-Pascual,[4] S. Masi,[2] Iván Mora-Seró[2*] and Carmen Coya[1*]*

[1] Dr. T. S. Ripolles, C. Redondo-Obispo, Prof. C. Coya
Escuela Técnica Superior de Ingeniería de Telecomunicación, Universidad Rey Juan Carlos, C/Tulipán s/n, 28933 Madrid, Spain.

E-mail: teresa.ripolles@urjc.es, carmen.coya@urjc.es

[2] P. Serafini, Dr. S. Masi, Prof. I. Mora-Seró
Institute of Advanced Materials (INAM), Universitat Jaume I, Castelló de la Plana, Av. Vicent Sos Baynat s/n, 12071, Spain.

E-mail: sero@uji.es

[3] C. D. Redondo-Obispo
Instituto de Ciencia de Materiales de Madrid, Consejo Superior de Investigaciones Científicas, C/ Sor Juana Inés de la Cruz 3, 28049 Madrid, Spain.

[4] Dr. E. Climent-Pascual
Escuela Técnica Superior de Ingenieros Industriales, Universidad Politécnica de Madrid, C/ José Gutiérrez Abascal 2, 28006 Madrid, Spain.

Keywords: halide perovskite, additive, phenethylammonium iodide, solar cell, passivation

Abstract:

In spite of the outstanding properties of metal halide perovskites, its polycrystalline nature induces a wide range of structural defects that results in charge losses that affect the final device performance and stability. In this work, a surface treatment is used to passivate interfacial vacancies and improve moisture tolerance. A functional organic molecule, phenylethyl ammonium iodide (PEAI) salt, is dissolved with the antisolvent step. The additive used at low concentration does not induce formation of low-dimensional perovskites species. Instead, the organic halide species passivate the surface of the perovskite and grain boundaries, which results in an effective passivation. For sake of generality, this facile solution-processed synthesis was studied for halide perovskite with different compositions, the standard perovskite $MAPbI_3$, and double cation perovskites, $MA_{0.9}Cs_{0.1}PbI_3$ and

$MA_{0.5}FA_{0.5}PbI_3$, increasing the average photoconversion efficiency (PCE) respect the reference cell by 18, 32 and 4 % respectively, observed for regular, n-i-p, and inverted, p-i-n, solar cell configurations. This analysis highlights the generality of this approach for halide perovskite materials in order to reduce non-radiative recombination as observed by impedance spectroscopy.

1. Introduction

Metal halide perovskite solar cells (PSCs) have attracted considerable attention due to their good light absorption, tunable band gap, long charge diffusion lengths, and low manufacturing costs.[1] To date, the highest power conversion efficiency (PCE) reported and certified has already exceeded 25.5 %,[2] being the most promising next-generation photovoltaic technologies in renewable energy. Interesting, this outstanding performance has been reached with polycrystalline thin films less demanding, from the industrial point view,[1b] than their crystalline counterparts. However, despite the benign defect physics of halide perovskites, the polycrystalline character of these materials leads to disorderly distribution of defects in the perovskite or at the grain boundaries, surfaces, and interfaces, that turns in losses of on the power conversion efficiency (PCE) of perovskite solar cells (PSCs).[3] Therefore, advances in passivating-strategies are highly demanded and would ensure a viable commercial future for PSCs. Recently, significant attention has been paid to improve the stability of PSCs via passivation of grain-boundary and interface engineering.[4]

To address this challenge, one of the most widely used passivating agents as additive is the organic halide salt phenylethyl ammonium iodide (PEAI).[4-5] This iodide salt is composed by two components, a bulky organic chain with a benzene ring and an ammonium group ($R\text{-}NH_3^+$) which represents PEA^+. Added to perovskite precursors, the large PEA^+ cation causes anionic layers in the 3D architecture to be isolated and transform into a 2D perovskite of general formula $(RNH_3)_2A_{n-1}B_nX_{3n+1}$ (n=1)[6] or into a quasi-3D perovskite compositions.[7]

The improved phase stability of the corresponding films, due to less defects at the grain boundaries,[8] efficiently increase the photovoltaic performance and the moisture stability of PSCs.[8-9] In addition, PEAI increases black phase stability,[10] as in all-inorganic perovskite $CsPbI_3$ stabilizing the orthorhombic black phase (γ-$CsPbI_3$) under ambient condition and to avoid the yellow δ-$CsPbI_3$ formation, achieving high open circuit voltage over 1.3 V.[11] Moreover, pure 2D $(PEA)_2PbI_4$ perovskite films prepared by blade-coating has an highly crystalline nature[12] and pure 2D $(PEA)_2SnI_4$ prepared by sequential vapor process of PEAI/SnI_2 shows less tendency to Sn oxidation.[13]

Besides, the PEA^+ cation has hydrophobic nature, which improves the moisture resistance of interfaces perovskite/transporting layers. In this sense, PEA^+ cation is considered an excellent additive if it is added properly in the 3D halide perovskite thin film. In fact, the PEAI salt was deposited as buffer layer in the PSCs[14] to control surface recombination. In particular, either on the top of the perovskite surface in order to retard the charge-carrier recombination process;[5b, 14b] or on the bottom of the perovskite layer to passivate defects of NiO_x and enhance the interface contact properties[5a] were successfully employed in p-i-n configuration. In all cases, PEAI-modified PSCs show better moisture resistance and superior thermal stability. Regarding n-i-p structure, a thin film of PEAI salt was deposited between perovskite $FA_{1-x}MA_xPbI_3$ and *spiro*-OMeTAD, to decrease surface defects and non-radiative recombination of halide perovskite films for efficient PSCs.[14a] The above-mentioned study demonstrated a high PCE of 23.34 %. PEAI salt was also studied in carbon electrode-based PSCs without hole transport materials to improve the poor perovskite/carbon contact. Specially, PEAI was added in a post-treatment carbon electrode once the PSC was prepared and PEAI film was deposited between the perovskite/carbon as an ultrathin PEA_2PbI_4 layer.[15] Due to the hydrophobic nature of carbon and 2D perovskite layers a large cell stability over 1000 h of exposure to ambient conditions was achieved.

However, this use of PEAI requires an additional fabrication step. Here, we propose to remove this further step by incorporating PEAI during the antisolvent step. The antisolvent additive engineering is another strategy to improve the perovskite structural properties and several additives have been used with success.[16] However, PEAI has been less explored in these conditions.[17] Bai *et al*. demonstrated a novel solution process to growth in situ a 2D layer together with 3D perovskite in order to suppress ion migration in the device and enhance the cell ambient stability. However, when 2D perovskite is synthetized, a balance between stability and efficiency is necessary due to the lower carrier mobility of 2D structure compared to 3D perovskites.[18]

Herein, we delve into the study of the PEAI effects caused in several metal halide compositions when the organic iodide salt is dissolved in the antisolvent at low concentration (0.0002-0.012 M). The experimental method proposed here avoid an additional step to fabricate a bilayer perovskite/PEAI composition which is typically used for this additive.[5a, 6-15] Instead, the PEAI is introduced in low concentrations. As far as we know, there is not references using this additive in such low amount, that it is an advantage in terms of material waste optimization. In order to study the generality of the approach, three different halide perovskite compositions, $MAPbI_3$, $MA_{0.9}Cs_{0.1}PbI_3$, and $MA_{0.5}FA_{0.5}PbI_3$, and two different solar cell structures, regular n-i-p and inverted p-i-n configurations, were deeply investigated and characterized. These materials have been selected as the two formers are broadly studied and present a tetragonal structure and the later because it presents a cubic structure, again for sake of the generality of the analysis. It was found that the introduction of the PEAI salt in the perovskite during the antisolvent step has an impact on reducing the crystallite domain size for all structures, as confirmed by XRD, and stabilizes their optical absorption up to 1300 h in ambient conditions. The role of the additive in the solar cells induces an increase of the PCE in all cases, as results of the reduction of the charge recombination processes confirmed by impedance spectroscopy.

2. Results and discussion

2.1. Perovskite film

We exploit the antisolvent additive engineering approach [16a] to introduce the PEAI salt at very low concentrations, 0.0002-0.012 M (see Experimental procedure for more details), in three representative metal halide perovskites compositions, mainly standard $MAPbI_3$, and double cation $MA_{0.9}Cs_{0.1}PbI_3$, and $MA_{0.5}FA_{0.5}PbI_3$. Henceforth, these perovskites are called MA, $MA_{0.9}Cs_{0.1}$, and $MA_{0.5}FA_{0.5}$, respectively.

Figure 1a-d shows the room temperature x-ray powder diffraction (XRD) profiles for the samples with different A-site compositions in the ABX_3 perovskite structure, with and without PEAI addition in the synthesis. The XRD data for all samples indicate that perovskite polycrystalline films were obtained for all compositions. The XRD profiles were indexed to an *I4cm* tetragonal cell for MA and $MA_{0.9}Cs_{0.1}$ since the small MA cation gives rise to tetragonal structures with elongation in the c axis. But changing the small MA cation for the larger FA cation (case $MA_{0.5}FA_{0.5}$) increases the Goldschmidt tolerance factor (t) beyond the tetragonal limit (t_{lim} = 0.972),[19] forming a cubic cell. In this case, $MA_{0.5}FA_{0.5}$ perovskite has been indexed to a Pm-3m cubic cell. The halide perovskite lattice parameters were refined by a profile matching approach (see **Figure S1**). For a better comparison of the obtained values, tetragonal parameters could be converted to pseudo-cubic parameters according to these equations: $a_{pc} = a_{tet}/\sqrt{2}$ and $c_{pc} = c_{tet}/2$. The lattice parameters as a function of the A-site composition could be seen in **Figure 1e**. In this figure, it can be seen how the presence of PEAI slightly increases the lattice parameters for the tetragonal compositions (MA and $MA_{0.9}Cs_{0.1}$), while it does not affect the cubic composition ($MA_{0.5}FA_{0.5}$).

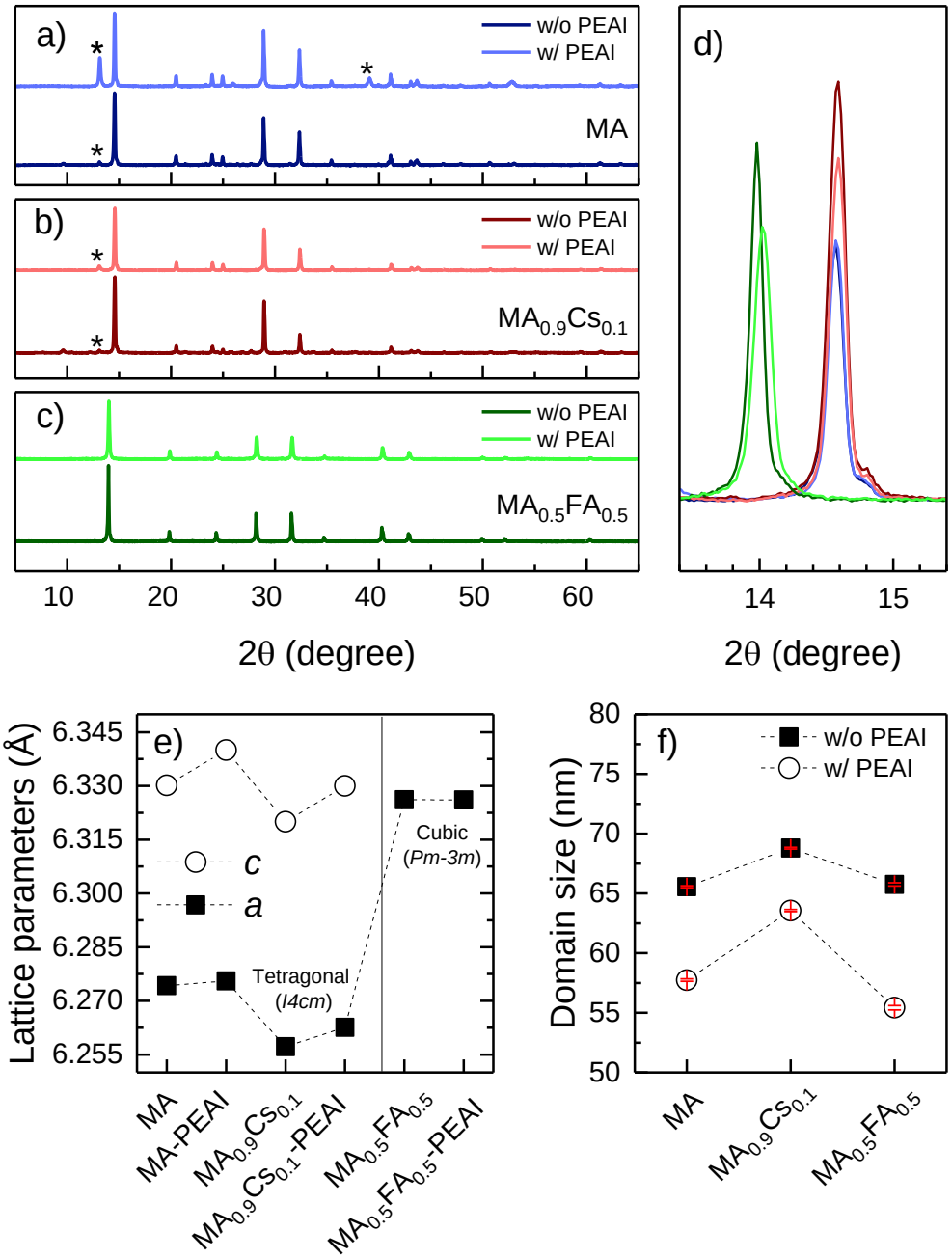

Figure 1. (a)-(c) XRD profiles (Cu Kα1/α2) of the MA, $MA_{0.9}Cs_{0.1}$ and $MA_{0.5}FA_{0.5}$ (with and without PEAI) films at 300 K. The asterisks indicate the impurity of PbI_2. (d) Zoom-in into the 13-16 2θ range. (e) Tetragonal *I4cm* (converted to pseudo-cubic) and cubic *Pm-3m* lattice parameters. (f) Variation of the average crystal domain size of samples with and without PEAI addition.

The average crystal domain size has been obtained using the Williamson-Hall (WH) methodology (**Figure S2**). The domain size as a function of the A-site composition in the films and the PEAI addition is shown in **Figure 1f**. PEAI reduces the crystallite size, likely indicative of more packed layers. When PEAI is not used, the domain size of MA and $MA_{0.5}FA_{0.5}$ is very similar (~65.6 nm), while it slightly increases to 68.8 nm (5 % increase) for the case of $MA_{0.9}Cs_{0.1}$. When PEAI is added, all domain sizes decrease, but the same trend is observed than without PEAI. To specify, there is a decrease of 11.9 %, 7.6 % and 15.8 %, with final values of 57.7 nm, 63.6 nm and 55.2 nm for MA, $MA_{0.9}Cs_{0.1}$ and $MA_{0.5}FA_{0.5}$, respectively.

The perovskite peak phase at 14.1º, which corresponds to the (110) reflection for MA and $MA_{0.9}Cs_{0.1}$ and to the (100) reflection for $MA_{0.5}FA_{0.5}$ have been followed over 1500 h by XRD of the perovskite layers under ambient conditions (see **Figure S3**). Interestingly, perovskite phase hardly changes with time and remains almost constant with the presence of PEAI.

The top-view scanning electron microscopy (SEM) images were carried out (see **Figure S4**). We found that the perovskite morphology was significantly altered by adding PEAI in the $MAPbI_3$ and $MA_{0.9}Cs_{0.1}PbI_3$ perovskites during the antisolvent, decreasing the grain size in both samples. At this point, it has to be noted that reducing the grain size is expected to be detrimental to efficiency due to recombination sites,[20] as grain boundaries are the major recombination sites in iodide-based perovskites.[21] However other effects should be considered as the grain boundary passivation. The result of a trade-off between these two effects can cause that lower size grains produce high performance devices as we observed by the addition of PEAI into the antisolvent step. The phase purity of the synthesized perovskite samples of bare $MAPbI_3$ perovskite and $MAPbI_3$ with iodide salt PEAI were verified by proton nuclear magnetic resonance (^{1}H NMR) spectroscopy. In order to have a net correspondence between the characterizations, we dissolved the prepared films in the proper

deuterated solvent (DMSO-d_6). Due to this preparation method the samples were quite diluted (**Figure S5a**) and the solvent peaks are predominant (DMSO and residual water). In **Figures S5b** and **S5c** it is clear the presence of the singlet corresponding to the ammonium group at 7.46 ppm and of the singlet from the aliphatic hydrogen of the MAI at 2.36 ppm respectively,[22] but there is no detectable trace of PEAI neither at high or low frequencies of the protonic spectra.[23] Each characteristic peak mentioned above is independent of the PEAI addition. Therefore, both samples maintain similar chemical environments, thus indicating that the PEAI is not incorporated into the perovskite structure. Considering on the other hand the effect in the morphology these studies point out to the grain boundaries for PEAI location.

In spite of the significant morphology changes induced by PEAI, in-plane DC dark resistivity (ρ) remains almost unaltered in the three compositions. The ρ-dependence with temperature in solar cells operation range temperature was measured for MA, $MA_{0.9}Cs_{0.1}$, and $MA_{0.5}FA_{0.5}$ thin films and is shown in **Figure S6**. The resistivity for MA and $MA_{0.9}Cs_{0.1}$ compositions are slightly reduced and $MA_{0.5}FA_{0.5}$ perovskite remains unaltered with PEAI addition in the cubic regime. This reduction in ρ could be associated with an increase in the packing of the layer and an improvement in the grain interfaces that favours charge transport. ρ values at room temperature are $1.2 \cdot 10^7$, $5.1 \cdot 10^6$ and $0.4 \cdot 10^6$ $\Omega \cdot$cm for pristine MA, $MA_{0.9}Cs_{0.1}$, and $MA_{0.5}FA_{0.5}$ perovskites, respectively, and, for perovskite thin films PEAI-doped are $2.4 \cdot 10^6$, $3.6 \cdot 10^6$ and $0.9 \cdot 10^6$ $\Omega \cdot$cm, respectively, in accordance with previous works for $MAPbI_3$ polycrystalline samples.[24]

The optical absorption spectra of bare perovskite and PEAI-doped perovskite samples are displayed in **Figure S7**. The local minima of the second derivatives of the optical density (O.D.) spectra is useful to estimate the optical transition energies,[25] which in this case, the first optical transition are located at 1.65 ± 0.04 eV for MA and $MA_{0.9}Cs_{0.1}$, and 1.59 ± 0.04 eV for $MA_{0.5}FA_{0.5}$, i.e. the optical band gap E_g, corresponding to the described direct

semiconductor type transitions at the R point in the pseudo-cubic Brillouin zone for perovskites.[26] The full width at half-maximum of the second derivative is assumed as the error. PEAI addition does not modify the optical band gap E_g, indicating that there are no changes in the stoichiometry of the synthesized thin films, in line with the NMR characterization. However, we found that the addition of PEAI has an important effect on the evolution of the absorption spectra under ambient conditions. In particular, the absorption coefficient remains constant up to 2.3 eV, which in concordance with the perovskite phase time evolution measured by XRD (**Figure S3** shows (110) peak evolution). Thus, it is confirmed that the PEAI salt stabilize the perovskite absorption in thin films over time, up to 1200 h, independently of the perovskite analyzed (**Figure S8**), especially in the $MA_{0.5}FA_{0.5}$ thin films (**Figure 2**), possibly helped by the more packed morphology.

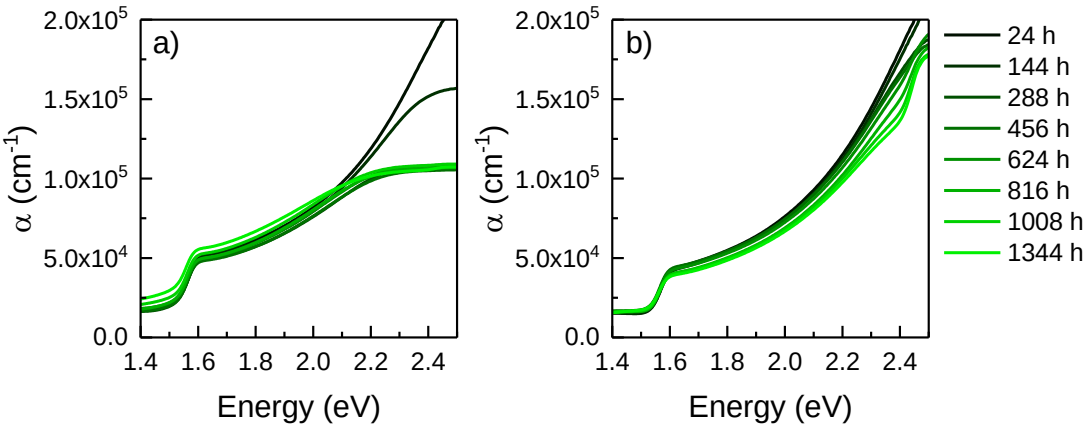

Figure 2. Absorption coefficient, α, over time of the $MA_{0.5}FA_{0.5}$ perovskite films, w/o (a) and w/PEAI (b) in the antisolvent solution.

Normalized photoluminescence (PL) emission for MA, $MA_{0.9}Cs_{0.1}$ and $MA_{0.5}FA_{0.5}$ thin films is represented in **Figure S7c**, and the maximum peak was located at 780, 770 and 807 nm, respectively, independently of the PEAI addition. These results are in line with the size of the cations introduced.[27] In addition, PL confocal microscopy (**Figure S9**) analyzed in an area of 20 × 20 μm^2 reveals high uniformity in the emission observed in the PL mapping images (**Figure S10**).

2.2. Perovskite device

To study the influence of PEAI salt on the photovoltaic performance, two types of solar cells were fabricated (see **Figure 3a**), in regular and inverted architectures to further generalize the method. The analyzed architectures are, regular for MA and $MA_{0.9}Cs_{0.1}$ (ITO/SnO_2/MA or $MA_{0.9}Cs_{0.1}$/*spiro*-OMeTAD/Au), and inverted for $MA_{0.5}FA_{0.5}$ (ITO/PEDOT:PSS/$MA_{0.5}FA_{0.5}$/PCBM/BCP/Al) (see SI for fabrication details).

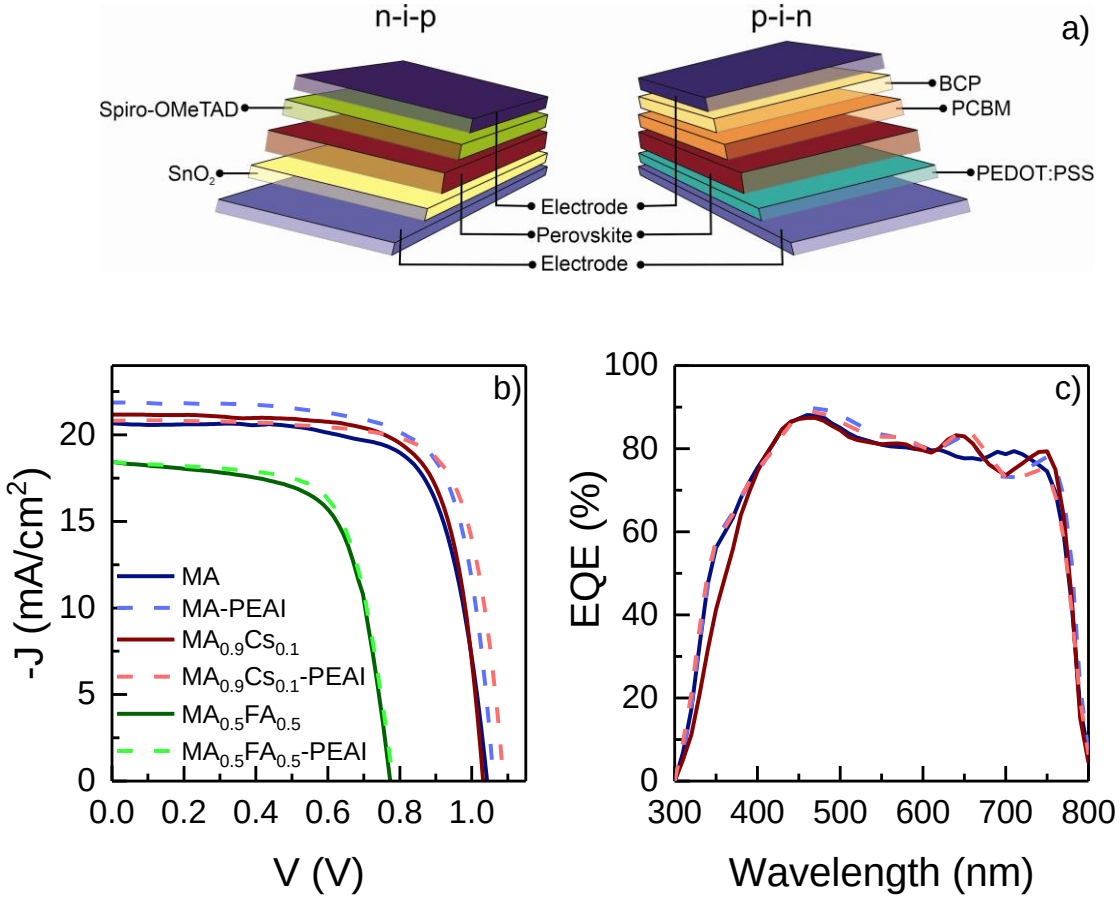

Figure 3. a) Device architectures n-i-p and p-i-n, b) photovoltage performance for champion devices under simulated 1 sun in forward sweep for the solar cells with (solid line) and without (dashed line) the salt PEAI effect, and c) EQE for the solar cells MA and $MA_{0.9}Cs_{0.1}$ perovskite compositions.

For the optimal PSCs, the J-V characteristics under a simulated air mass (AM) of 1 sun illumination (100 mW/cm^2) are shown in **Figure 3b**, and the corresponding photovoltaic parameters are summarized in Table 1.

Table 1. Photovoltaic parameters of the p-i-n and n-i-p PSCs based on PEAI salt. It is included the champion solar cell and the average values with standard errors from 10 devices fabricated in parallel.

Perovskite	Architecture	V_{oc} (V)	J_{sc} (mA/cm^2)	FF (%)	PCE (%)
MA	n-i-p	1.043 (1.02 ± 0.02)	20.685 (20.5 ± 0.6)	71.2 (62 ± 5)	15.35 (12.9 ± 1.4)
MA-PEAI	n-i-p	1.06 (1.07 ± 0.01)	21.86 (20.7 ± 1.0)	72.4 (69 ± 3)	16.77 (15.2 ± 1.2)
$MA_{0.9}Cs_{0.1}$	n-i-p	1.031 (1.01 ± 0.02)	21.143 (20.2 ± 0.6)	72.6 (59 ± 7)	15.83 (12.1 ± 2.0)
$MA_{0.9}Cs_{0.1}$-PEAI	n-i-p	1.088 (1.07 ± 0.01)	20.83 (21.0 ± 0.5)	74.3 (71 ± 3)	16.84 (16.0 ± 1.0)
$MA_{0.5}FA_{0.5}$	p-i-n	0.773 (0.780 ± 0.006)	18.44 (16.3 ± 1.8)	66.10 (65.4 ± 2.0)	9.42 (8.3 ± 0.9)
$MA_{0.5}FA_{0.5}$-PEAI	p-i-n	0.781 (0.780 ± 0.005)	18.42 (16.8 ± 1.3)	68.15 (66.5 ± 2.5)	9.80 (8.7 ± 0.8)

A positive significant impact is observed on the photovoltaic performance with PEAI salt addition in the antisolvent, independently of the active layer used, MA, $MA_{0.9}Cs_{0.1}$, and $MA_{0.5}FA_{0.5}$, and the architecture of the PSCs, either regular or inverted. Table 1 includes the statistical photovoltaic parameters of 10 devices fabricated from different branches. It can be seen that these devices exhibit good reproducibility. In particular, $MA_{0.9}Cs_{0.1}$-PEAI based PSCs have a higher average efficiency among these PSCs, from 12.06 % in pristine PSCs to 15.97 % in $MA_{0.9}Cs_{0.1}$-PEAI PSCs.

As we expected from the optical band gap E_g, the $MA_{0.5}FA_{0.5}$-based solar cells displayed lower open-circuit voltage, V_{oc}, close to 0.78 V, and an enhancement of V_{oc} for MA- and

$MA_{0.9}Cs_{0.1}$-based solar cells over 1 V, however these values are also influence by the architecture and recombination processes. Interestingly, a V_{oc} increment is observed for all PEAI-based PSCs, which could be associated with a lower recombination rate,[28] as pointed out later by impedance spectroscopy analysis. Same behaviour was observed to short-circuit current, J_{sc}, and fill factor, FF, being the highest results for $MA_{0.9}Cs_{0.1}$-based PSC to J_{sc} over 21 mA/cm^2 and FF of 74.3 %. **Figure 3c** presents the external quantum efficiency (EQE) spectrum of the regular PSCs. The photocurrent density was integrated from the spectrum (see **Figure S11**), which reveals that the J_{sc} with a value of 20.23, 20.59, 20.19, and 20.38 mA/cm^2 for PSCs of MA, MA-PEAI, $MA_{0.9}Cs_{0.1}$, $MA_{0.9}Cs_{0.1}$-PEAI, respectively. J_{sc} obtained from the J-V measurement and the EQE spectrum are in good agreement, with a difference less than 5 %.

As can be observed in **Figure 3b**, the PEAI treatment increases the performance of champion cells for all the analysed materials and architectures, increasing PCE of PEAI treated MA, $MA_{0.9}Cs_{0.1}$ and $MA_{0.5}FA_{0.5}$ champion cells respect reference by 9, 6 and 4 %, respectively. Interestingly, for MA and $MA_{0.9}Cs_{0.1}$, the most efficient ones, average PCE is more significantly enhanced by 18 and 32 %, respectively.

In order to further investigate the effect of PEAI treatment, impedance spectroscopy has been measured at open circuit conditions with different light intensities for MA- and $MA_{0.9}Cs_{0.1}$-based solar cells.[29] The Nyquist plots at V_{oc} of impedance spectra at 1 sun are represented in **Error! No s'ha trobat l'origen de la referència.a**. As it is conventionally observed in high efficient PSCs, we observed mainly two different semicircles, at low frequency (LF) and high frequency (HF) ranges. In both devices measured it is observed a decrease in width of the arc when PEAI is used which indicates a lower resistance or better transport due to the presence of the cation at grain boundary as mentioned before which will result in higher PCE. In order to analyze more careful these data, an equivalent circuit model previously reported has been used and it is represented in **Figure 4b**.[30] In particular, the recombination resistance, $R_{rec,}$ see

Figure 4c, has been obtained by the fitting of impedance measurements, as the sum of the resistances of high and low frequency arcs, considering transport resistance negligible.[30] It can be observed that independently of the halide perovskite layer, PEAI treatment increases recombination resistance, and consequently indicates a decrease of the non-radiative recombination rate. The process of recombination losses is reduced efficiently by PEAI addition, in concordance with the observed V_{oc} increment. The PEAI salt, despite the low concentrations, induces a grain boundary halide perovskite passivation and a reduction of interfacial recombination. Interestingly, the long-term stability is also slightly enhanced despites the low amount of additive, see **Figure S12** and **S13**.

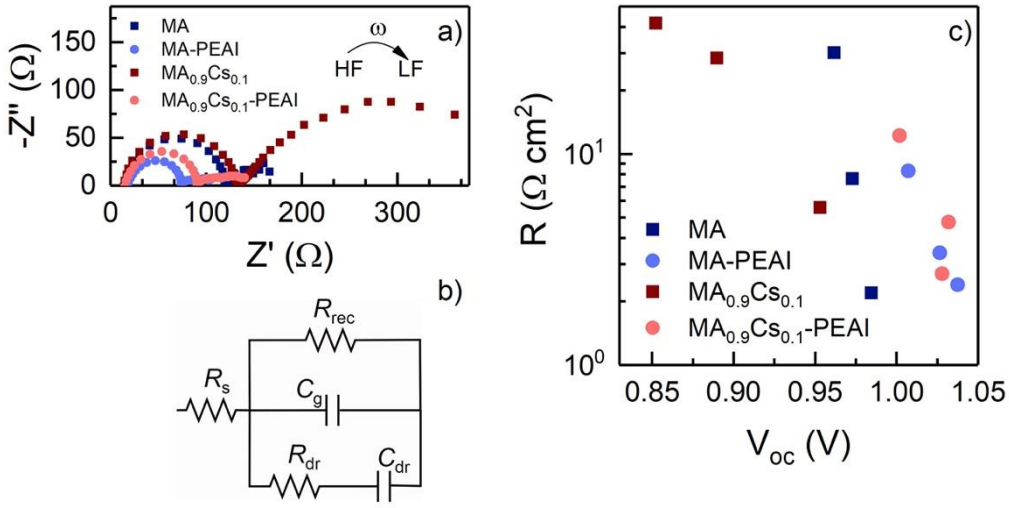

Figure 4. a) Nyquist plots at open circuit voltage under 1 sun illumination intensity, b) equivalent circuit model composed of a series resistance, R_s, recombination resistance, R_{rec}, obtained as the sum of HF and LF arcs, considering the transport resistance negligible, which is in parallel to a HF capacitance, C_g, the geometrical capacitance, an in parallel with a RC branch (C_{dr} and R_{dr}), that splits the pattern in the HF and LF arcs,[32] and c) recombination resistance at open circuit conditions for the PSCs w/o and w/PEAI in regular architecture.

3. Conclusions

In summary, we have demonstrated that adding PEAI salt at low concentration during the antisolvent step is one alternative to improve perovskite solar cells performance, without increasing the number of fabrication steps. The proposed method is tested in three representative compositions, the standard perovskite $MAPbI_3$, and double cation perovskites, $MA_{0.9}Cs_{0.1}PbI_3$ and $MA_{0.5}FA_{0.5}PbI_3$, and both, regular and inverted solar cells. PEAI reduces the crystallite domain size, enhancing the morphology. XRD and optical absorption confirms a stabilization effect of the perovskite phase in thin films for all compositions. For solar devices, the addition of PEAI leads to a PCEs increase, respect reference cells without treatment, by a very significant 18 and 32 % for MA and $MA_{0.9}Cs_{0.1}$ respectively and by a 4 % for $MA_{0.5}FA_{0.5}$, and to a reduction of the recombination rate in all the cases. Besides, from NMR analysis, PEAI is not incorporated into the halide perovskite structure, reinforcing their passivating role at the grain boundaries, reducing traps states which results in the observed higher V_{oc}. Those findings found for a broad range of halide perovskite materials, with both tetragonal and cubic phase, and for both regular and inverted architectures, highlighting the generality of the simple approach. Decreasing the number of fabrication steps would have an important effect in the environmental impacts and cost of large-scale perovskite fabrication.

4. Experimental procedure

4.1. Synthesis

Materials: All materials were reagent grade and were used as received. Perovskite precursors are lead iodide (PbI_2, > 98 %, from TCI and Aldrich) and methylammonium iodide (MAI, 98 %, from Greatcellsolar and Dyesol). The solvents used are 2-propanol (99.7 % from Carlo

Erba), ethanol (96 %) and acetone (99.25 %) from PanReac, dimethyl formamide (DMF anhydrous 99.9 %), dimethyl sulfoxide (DMSO anhydrous 99.9 %), clorobenzene (CB anhydrous 99.8 %), acetonitrile (MeCN anhydrous 99.8 %), ethylacetate (EA anhydrous 99.8%), 4-tert-butylpiridine (TBP 96 %), zinc powder (99.995 %) and lithium bis(trifluoromethylsulfonyl)imide (Li-TFSI, 99.95 %) from Sigma Aldrich. 2,20,7,70-tetrakis [N,N-di(4-methoxyphenyl)amino]-9,90-*spiro*bifluorene (*spiro*-OMeTAD 99 %) from Feiming chemical limited. The hydrochloric acid (HCl 37 %) is from Aldrich. The electron transport layer such as SnO_2 colloid precursor is from Alfa Aesar (15 % in H_2O colloidal dispersion) and PCBM is from Aldrich (>99.8 %). The hole transport layer PEDOT:PSS Clevious P VP AI 4083 aqueous solution is from Heraeus. Indium tin oxide (ITO) coated glass substrates (Pilkington TEC15, ~ 15 Ω sq^{-1}).

Preparation of perovskite solutions: Three compositions have been synthesized, such as $MAPbI_3$, $MA_{0.9}Cs_{0.1}PbI_3$ and $MA_{0.5}FA_{0.5}PbI_3$. The solution preparation of each composition is as follow. Perovskite $MAPbI_3$ was prepared with a mixture of perovskite precursors of PbI_2 and MAI with a concentration of 1.4 M for each precursor and solved with a mixture of solvents, DMF:DMSO (4:1, v:v). Perovskite $MA_{0.9}Cs_{0.1}PbI_3$ follows the same trend than the perovskite standard $MAPbI_3$ and the precursor CsI is added with a concentration of 1.4 M and the precursors were solved with pure DMSO. The perovskite composition $MA_{0.5}FA_{0.5}PbI_3$ with a concentration of 0.65 M was prepared with a mixture of PbI_2, MAI and FAI and dissolved with DMF:DMSO (4:1, v:v).

4.2. Device fabrication n-i-p

Structure ITO/SnO_2/$MAPbI_3$ or $MA_{0.9}Cs_{0.1}PbI_3$/*spiro*-OMeTAD/Au. Glass substrates coated with ITO were etched by using zinc powder and pour over it drops of HCl 2 M. Then, glass was cleaned with deionized water, acetone and ethanol in an ultrasonic cleaner for 15 min for each solvent one after the other. After being dried by air flow, the substrates were treated in

an ultraviolet-ozone (UV-O_3) for 15 min to remove organic residues. Once the substrates were cleaned, the electron transport layer ETL SnO_2 was deposited in ambient at 25 °C and 30 % RH by preparing a solution of SnO_2 3 % in water from the Alfa Aesar solution of 15 %. The ETL was spin-coated onto the ITO substrates with a speed of 3000 rpm for 30 s, and then heated at 150 °C for 30 min. Once the SnO_2 film was prepared, the substrates were submitted to 20 min of UV-O_3 previously to perovskite deposition inside glovebox. A quantity of 50 μL of perovskite was deposited over SnO_2 film by one-step spin coating at 4000 rpm for 20 s. At 8 s after starting the second step, an aliquot of 400 μL was added, either toluene or PEAI filtered solution with a concentration of 0.05 mg/mL. As soon as the spin coating was finished, the sample was moved to a hotplate at 130 ºC for 10 min. After perovskite preparation, a 50 μL of hole transporting layer HTL (*spiro*-OMeTAD) solved in chlorobenzene (85.5 mg/mL) doped with 28.8 μL of TBP and 17.8 μL of a stock solution of 520 mg/mL of Li-TFSI in acetonitrile was spin-coated at 4000 rpm for 20 s onto the top annealed perovskite layers. Finally, Au electrode was deposited by thermal evaporation with a thickness of 80 nm.

4.3. Device fabrication p-i-n

Structure ITO/PEDOT:PSS/$MA_{0.5}FA_{0.5}PbI_3$/PCBM/BCP/Al. Glass substrates patterned with ITO were treated in the same way than in the proceeding described previously. Once the substrates were completely cleaned, the next steps were carried out in the glove box filled with nitrogen until end of the procedure. A diluted PEDOT:PSS solution (PEDOT:PSS:2-propanol, 5:1, v:v) were deposited by spin coater 4000 rpm for 45 s. Then, the HTL were heated at 130 ºC for 30 min. The perovskite solution (150 μL) was dropped onto the PEDOT:PSS film and then spin coated at 1000 rpm for 10 s and then, at 6000 rpm for 30 s. As has been mentioned, the anti-solvent method used includes at 15 s of the second step add 450 μL either EA or PEAI filtered solution (0.05 mg/mL solved with EA). The perovskite

films were kept at room temperature for 30 min and then heated at 100 ºC for 40 min. The ETL was formed by spin coating a solution of PCBM in CB (40 mg/mL) of 2000 rpm for 40 s and then, the film was treated at 60 ºC for 10 min. On the top of the PCBM, a thin layer of BCP (5 mg/mL in 2-propanol) was added by spin coater as 5000 rpm for 40 s. Finally, a thermal evaporation was carried out to evaporate Al.

4.4. Film characterization

X-Ray Diffraction (XRD): The XRD diffractograms of the perovskite thin films were measured by Bruker D8 Advance diffractometer using Cu K_α radiation over a 2θ range between 5° and 65° with a step size of 0.02°.

Optical characterization: UV-Vis absorption of the thin films was characterized using a UV-VIS-NIR spectrophotometer (Varian, Cary 5000) in the wavelength range of 300-900 nm.

Steady state photoluminescence emission (PL): confocal PL emission was measured with an inverted confocal microscope Leica TCS SP8 using an excitation wavelength of 561 nm with DPSS 561 laser employing a spectral resolution of 5 nm and 63 times of zoom image.

Electrical characterization: In-plane DC dark resistivity-temperature dependence was obtained from current-voltage characteristics with two-wire configuration due to the high resistance of the samples and a homemade Faradaic box. The dependences with increasing temperature have been measured in the 298-373 K range, with 10 K step size. The samples (thin films on glass substrate) were located on a hot plate with a K–type thermocouple right beside the sample to a process controller Electemp-TFT (Selecta). Current-voltage curves were measured at each temperature after 3 min stabilization, using a probe station and a Keithley 2450 Sourcemeterb between two evaporated Aluminium contacts.

Scanning electron microscopy (SEM): SEM measurements were used to analyse the perovskite surface by employing a JEOL 7001F microscope with an electron gun of 0.1 – 30 kV power which allow us to obtain an image at 20.000 times magnification.

Hydrogen Nuclear magnetic resonance (H-NMR): NMR measurements were taken using a spectrometer Bruker Avance III HD 400 MHz employing solutions dissolved in DMSO-d_6 to analyze chemical shift between 0-10 ppm.

4.5. Device characterization

Current-voltage (J-V) measurement: J-V measurements were performed under AM 1.5G (100 mW/cm^2) conditions with a Wavelabs Sinus-70 AAA LED solar simulator with a Keithley 2450 sourcemeter. Each J-V curve was carried out from 0 V to 1.15 V (forward direction) in a scan rate of 90 mV/s without preconditioning. The spectrum of the solar simulator is monitored with reference intensity sensor in test plane in combination with fast feedback loop for automatic intensity correction and temperature control for the LEDs. The aging test was evaluated keeping the PSCs under dark and N_2 atmosphere.

Incident photon to current efficiency (IPCE): IPCE measurements were performed using a Xenon lamp with a monochromator Oriel Cornestone 130 which was used to measure along the wavelength of the spectrum. Prior measurement, calibration was done using a reference photodiode of silicon and each measurement was obtained using TRACQ BASIC software. Finally, EQE scans were taken from 300 nm to 810 nm every 10 nm.

Impedance spectroscopy: The IS was measured using a Potentiostat Autolab-PGSTAT204 in open circuit conditions. The light intensity was controlled by the Wavelabs Sinus-70 AAA LED solar simulator. For each light intensity, an AC 20 mV voltage perturbation was carried out and the frequency range was from 1 MHz to 100 mHz. Z-View software was used to fit the impedance spectra.

Supporting Information. Details of experiments and additional supplementary figures. This material is available free of charge via the Internet.

ACKNOWLEDGMENT

T.S.R. acknowledges funding from Community of Madrid under the Talent fellowship 2017-T2/IND-5586 and project F660 financed by Community of Madrid and Rey Juan Carlos University. We acknowledge financial support by the Spanish Ministry of Science and Innovation under Projects PID2020-115514RB-I00, MAT2015-65356-C3-2-R, and PID2019-107314RB-I00. This work was partially supported by European Research Council (ERC) via Consolidator Grant (724424–No-LIMIT), AYUDA PUENTE 2020 URJC. Associated Lab LABCADIO belonging to CM net laboratories ref 351 are also acknowledge. C.R.O. acknowledges funding from the Spanish Ministry of Science and Innovation under a FPI pre-doctoral contract (PRE2019-088433).

Received: ((will be filled in by the editorial staff))
Revised: ((will be filled in by the editorial staff))
Published online: ((will be filled in by the editorial staff))

References

[1] a) J. Y. Kim, J.-W. Lee, H. S. Jung, H. Shin, N.-G. Park, *Chemical Reviews* **2020**, 120, 7867; b) R. Vidal, J.-A. Alberola-Borràs, N. Sánchez-Pantoja, I. Mora-Seró, *Advanced Energy and Sustainability Research* **2021**, 2, 2000088.

[2] M. Green, E. Dunlop, J. Hohl-Ebinger, M. Yoshita, N. Kopidakis, X. Hao, *Progress in Photovoltaics: Research and Applications* **2021**, 29, 3.

[3] F. Gao, Y. Zhao, X. Zhang, J. You, *Advanced Energy Materials* **2020**, 10, 1902650.

[4] a) Y. Gao, Y. Wu, Y. Liu, M. Lu, L. Yang, Y. Wang, W. W. Yu, X. Bai, Y. Zhang, Q. Dai, *Nanoscale Horizons* **2020**, 5, 1574; b) P. Guo, Q. Ye, X. Yang, J. Zhang, F. Xu, D. Shchukin, B. Wei, H. Wang, *Journal of Materials Chemistry A* **2019**, 7, 2497.

[5] a) Y. Liu, J. Duan, J. Zhang, S. Huang, W. Ou-Yang, Q. Bao, Z. Sun, X. Chen, *ACS Applied Materials & Interfaces* **2020**, 12, 771; b) F. Zhang, Q. Huang, J. Song, Y. Zhang, C. Ding, F. Liu, D. Liu, X. Li, H. Yasuda, K. Yoshida, J. Qu, S. Hayase, T. Toyoda, T. Minemoto, Q. Shen, *Solar RRL* **2020**, 4, 1900243.

[6] J. Zhang, X. Zhu, M. Wang, B. Hu, *Nature Communications* **2020**, 11, 2618.

[7] C. Zuo, A. D. Scully, W. L. Tan, F. Zheng, K. P. Ghiggino, D. Vak, H. Weerasinghe, C. R. McNeill, D. Angmo, A. S. R. Chesman, M. Gao, *Communications Materials* **2020**, 1, 33.

[8] N. Li, Z. Zhu, C.-C. Chueh, H. Liu, B. Peng, A. Petrone, X. Li, L. Wang, A. K. Y. Jen, *Advanced Energy Materials* **2017**, 7, 1601307.

[9] L. Zhou, Z. Lin, Z. Ning, T. Li, X. Guo, J. Ma, J. Su, C. Zhang, J. Zhang, S. Liu, J. Chang, Y. Hao, *Solar RRL* **2019**, 3, 1900293.
[10] S. Masi, A. F. Gualdrón-Reyes, I. Mora-Seró, *ACS Energy Letters* **2020**, 5, 1974.
[11] Q. Ye, F. Ma, Y. Zhao, S. Yu, Z. Chu, P. Gao, X. Zhang, J. You, *Small* **2020**, 16, 2005246.
[12] H. Duim, G. H. ten Brink, S. Adjokatse, R. de Kloe, B. J. Kooi, G. Portale, M. A. Loi, *Small Structures* **2020**, 1, 2000074.
[13] W.-G. Choi, C.-G. Park, Y. Kim, T. Moon, *ACS Energy Letters* **2020**, 5, 3461.
[14] a) Q. Jiang, Y. Zhao, X. Zhang, X. Yang, Y. Chen, Z. Chu, Q. Ye, X. Li, Z. Yin, J. You, *Nature Photonics* **2019**, 13, 460; b) B. Li, Y. Xiang, K. D. G. I. Jayawardena, D. Luo, Z. Wang, X. Yang, J. F. Watts, S. Hinder, M. T. Sajjad, T. Webb, H. Luo, I. Marko, H. Li, S. A. J. Thomson, R. Zhu, G. Shao, S. J. Sweeney, S. R. P. Silva, W. Zhang, *Nano Energy* **2020**, 78, 105249.
[15] K. Lee, J. Kim, H. Yu, J. W. Lee, C.-M. Yoon, S. K. Kim, J. Jang, *Journal of Materials Chemistry A* **2018**, 6, 24560.
[16] a) T. T. Ngo, I. Suarez, G. Antonicelli, D. Cortizo-Lacalle, J. P. Martinez-Pastor, A. Mateo-Alonso, I. Mora-Sero, *Advanced Materials* **2017**, 29, 1604056; b) Y.-J. Kang, S.-N. Kwon, S.-P. Cho, Y.-H. Seo, M.-J. Choi, S.-S. Kim, S.-I. Na, *ACS Energy Letters* **2020**, 5, 2535.
[17] Y. Bai, S. Xiao, C. Hu, T. Zhang, X. Meng, H. Lin, Y. Yang, S. Yang, *Advanced Energy Materials* **2017**, 7, 1701038.
[18] S. Zhang, S. M. Hosseini, R. Gunder, A. Petsiuk, P. Caprioglio, C. M. Wolff, S. Shoaee, P. Meredith, S. Schorr, T. Unold, P. L. Burn, D. Neher, M. Stolterfoht, *Advanced Materials* **2019**, 31, 1901090.
[19] W. Li, M. U. Rothmann, Y. Zhu, W. Chen, C. Yang, Y. Yuan, Y. Y. Choo, X. Wen, Y.-B. Cheng, U. Bach, J. Etheridge, *Nature Energy* **2021**, 6, 624.
[20] H. D. Kim, H. Ohkita, H. Benten, S. Ito, *Advanced Materials* **2016**, 28, 917.
[21] R. Long, J. Liu, O. V. Prezhdo, *Journal of the American Chemical Society* **2016**, 138, 3884.
[22] S. Masi, F. Aiello, A. Listorti, F. Balzano, D. Altamura, C. Giannini, R. Caliandro, G. Uccello-Barretta, A. Rizzo, S. Colella, *Chemical Science* **2018**, 9, 3200.
[23] G. Min, Y. Yun, H.-J. Choi, S. Lee, J. Joo, *Journal of Industrial and Engineering Chemistry* **2020**, 89, 375.
[24] a) C. C. Stoumpos, C. D. Malliakas, M. G. Kanatzidis, *Inorganic Chemistry* **2013**, 52, 9019; b) A. Pisoni, J. Jaćimović, O. S. Barišić, M. Spina, R. Gaál, L. Forró, E. Horváth, *The Journal of Physical Chemistry Letters* **2014**, 5, 2488.
[25] a) C. Coya, C. Ruiz, Á. L. Álvarez, S. Álvarez-García, E. M. García-Frutos, B. Gómez-Lor, A. de Andrés, *Organic Electronics* **2012**, 13, 2138; b) J. Bartolomé, E. Climent-Pascual, C. Redondo-Obispo, C. Zaldo, Á. L. Álvarez, A. de Andrés, C. Coya, *Chemistry of Materials* **2019**, 31, 3662.
[26] a) M. Shirayama, H. Kadowaki, T. Miyadera, T. Sugita, M. Tamakoshi, M. Kato, T. Fujiseki, D. Murata, S. Hara, T. N. Murakami, S. Fujimoto, M. Chikamatsu, H. Fujiwara, *Physical Review Applied* **2016**, 5, 014012; b) A. M. A. Leguy, P. Azarhoosh, M. I. Alonso, M. Campoy-Quiles, O. J. Weber, J. Yao, D. Bryant, M. T. Weller, J. Nelson, A. Walsh, M. van Schilfgaarde, P. R. F. Barnes, *Nanoscale* **2016**, 8, 6317.
[27] a) Y. Zhang, G. Grancini, Y. Feng, A. M. Asiri, M. K. Nazeeruddin, *ACS Energy Letters* **2017**, 2, 802; b) Y. Chang, L. Wang, J. Zhang, Z. Zhou, C. Li, B. Chen, L. Etgar, G. Cui, S. Pang, *Journal of Materials Chemistry A* **2017**, 5, 4803.
[28] W. Tress, N. Marinova, O. Inganäs, M. K. Nazeeruddin, S. M. Zakeeruddin, M. Graetzel, *Advanced Energy Materials* **2015**, 5, 1400812.

[29] D. Pitarch-Tena, T. T. Ngo, M. Vallés-Pelarda, T. Pauporté, I. Mora-Seró, *ACS Energy Letters* **2018**, 3, 1044.
[30] S.-M. Yoo, S. J. Yoon, J. A. Anta, H. J. Lee, P. P. Boix, I. Mora-Seró, *Joule* **2019**, 3, 2535.

The table of contents

An effective perovskite surface passivation is investigated by adding an organic molecule phenylethyl ammonium iodide (PEAI) salt solved in the antisolvent. This facile method is used in different perovskite compositions, $MAPbI_3$, $MA_{0.9}Cs_{0.1}PbI_3$ and $MA_{0.5}FA_{0.5}PbI_3$, and architectures, regular and inverted. The PEAI-based solar cell shows higher photoconvertion efficiencies and a reduction of the non-radiative recombination processes which favors a promising future view.

T. S. Ripolles,[1†] Patricio Serafini,[2†] Carlos Redondo-Obispo,[1,3] Esteban Climent-Pascual,[4] S. Masi,[2] Iván Mora-Seró[2*] and Carmen Coya[1*]*

Interface Engineering in Perovskite Solar Cells by low concentration of PEAI solution in the antisolvent step

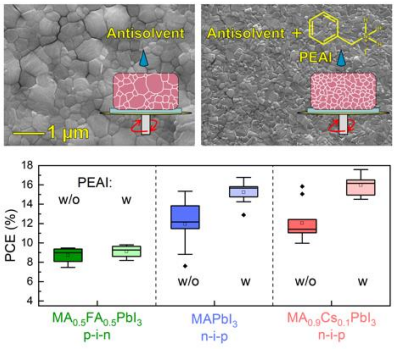

Supporting Information

Interface Engineering in Perovskite Solar Cells by low concentration of PEAI solution in the antisolvent step

T. S. Ripolles,[1†] Patricio Serafini,[2†] Carlos Redondo-Obispo,[1,3] Esteban Climent-Pascual,[4] S. Masi,[2] Iván Mora-Seró[2*] and Carmen Coya[1*]*

Figure contents

Supporting Figures

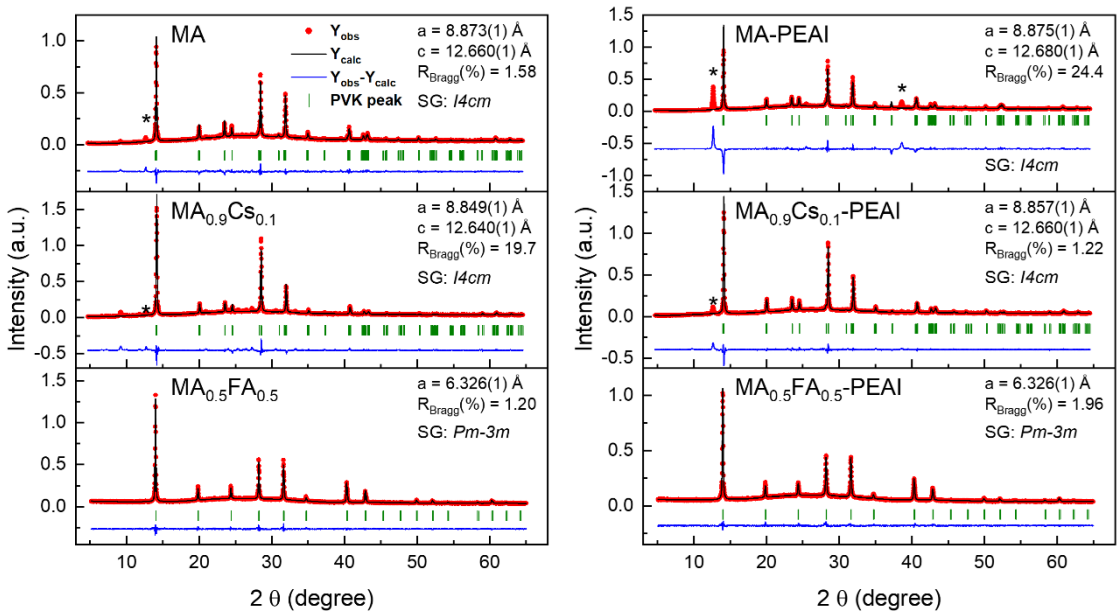

Figure S1. Profile matching fits (solid black line) of XRD (Cu Kα1/α2) data (red circles) of the films at 300 K. Green tick marks indicate the position of allowed tetragonal *I4cm* (MA and $MA_{0.9}Cs_{0.1}$) and cubic *Pm-3m* ($MA_{0.5}FA_{0.5}$). The asterisks indicate the impurity of PbI_2.The Bragg R-factor (%) and the space group (SG) for the samples is also included. Profile matching made using FullProf software.

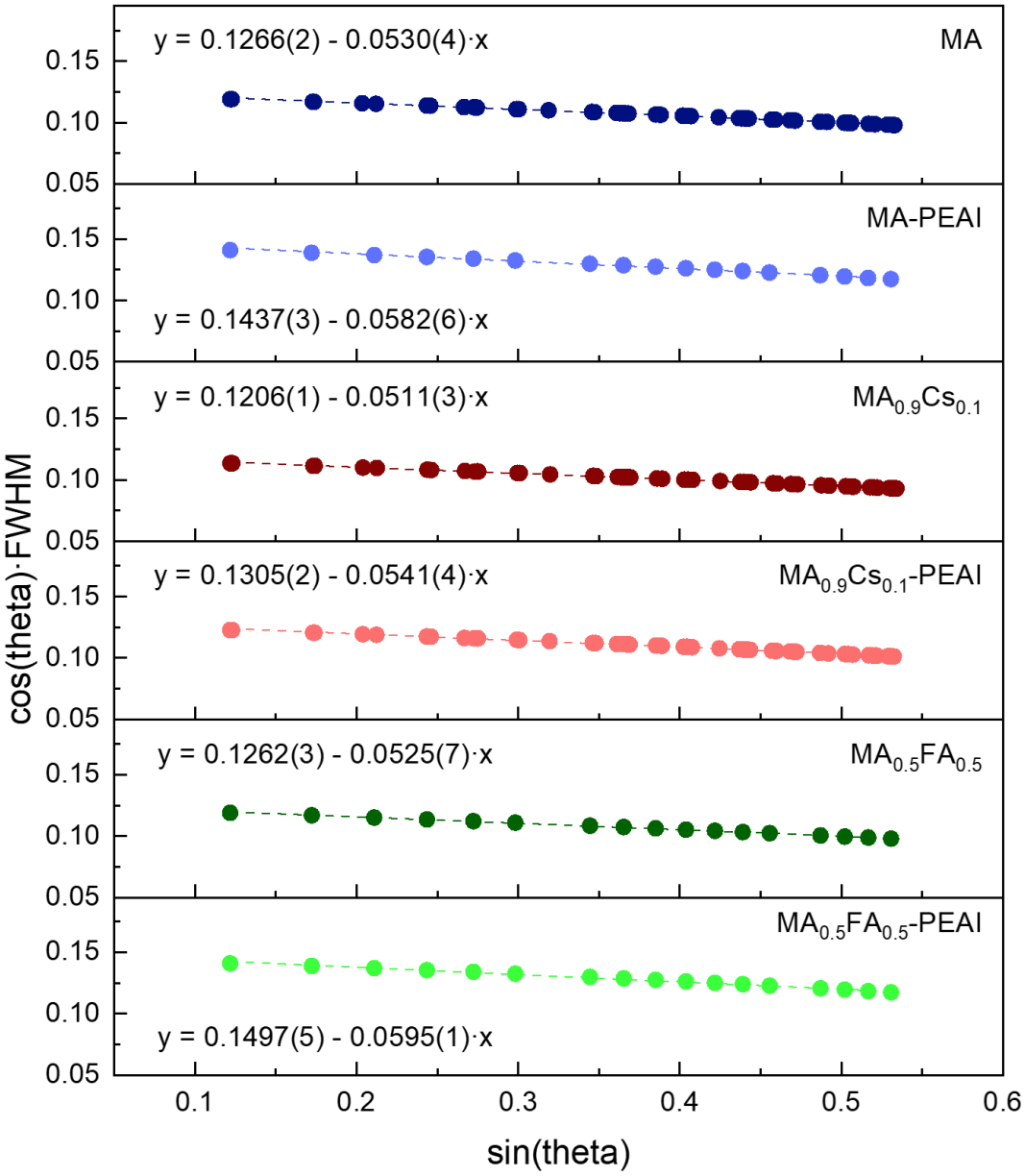

Figure S2. Williamson-Hall plots for all films under study.

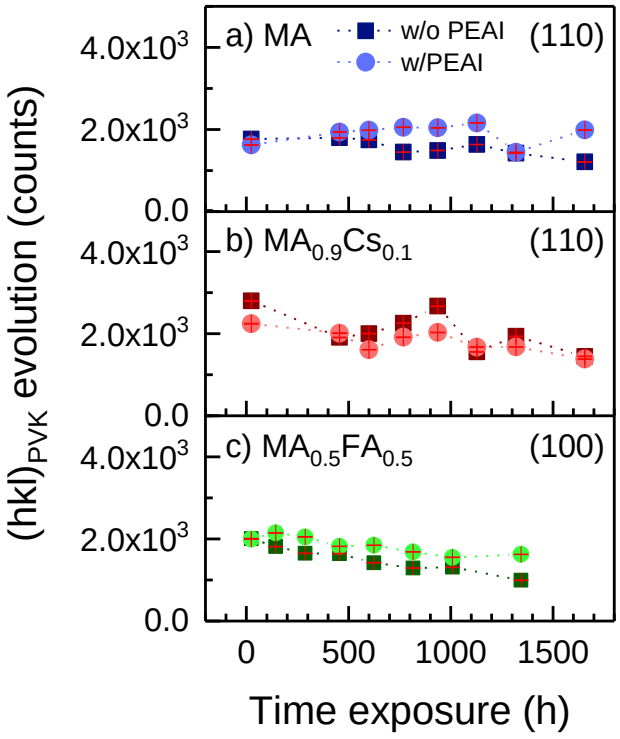

Figure S3. Evolution of the (a-c) main perovskite peak intensity at 14.1º ((110) for MA and $MA_{0.9}Cs_{0.1}$ and (100) for $MA_{0.5}FA_{0.5}$) for pristine films (square dots) and w/PEAI based perovskite films (circle dots).

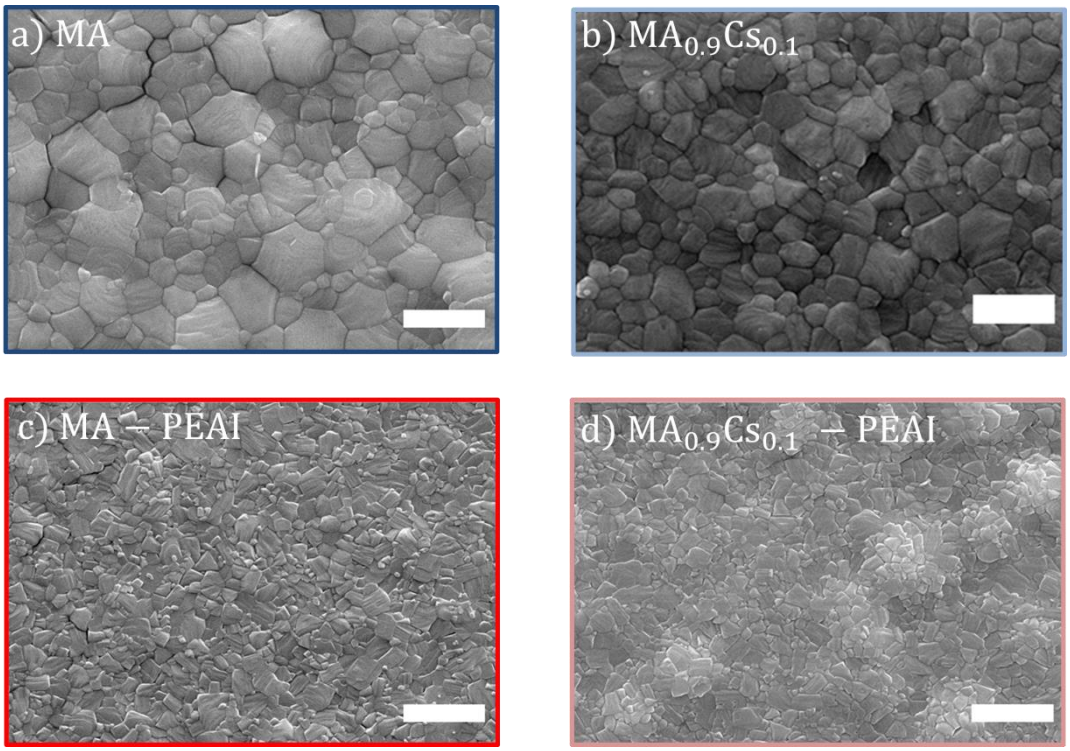

Figure S4. Top-view SEM images of MA and $MA_{0.9}Cs_{0.1}$ perovskites w/o and w/PEAI. The substrate was glass/ITO. The bar size is 1 μm.

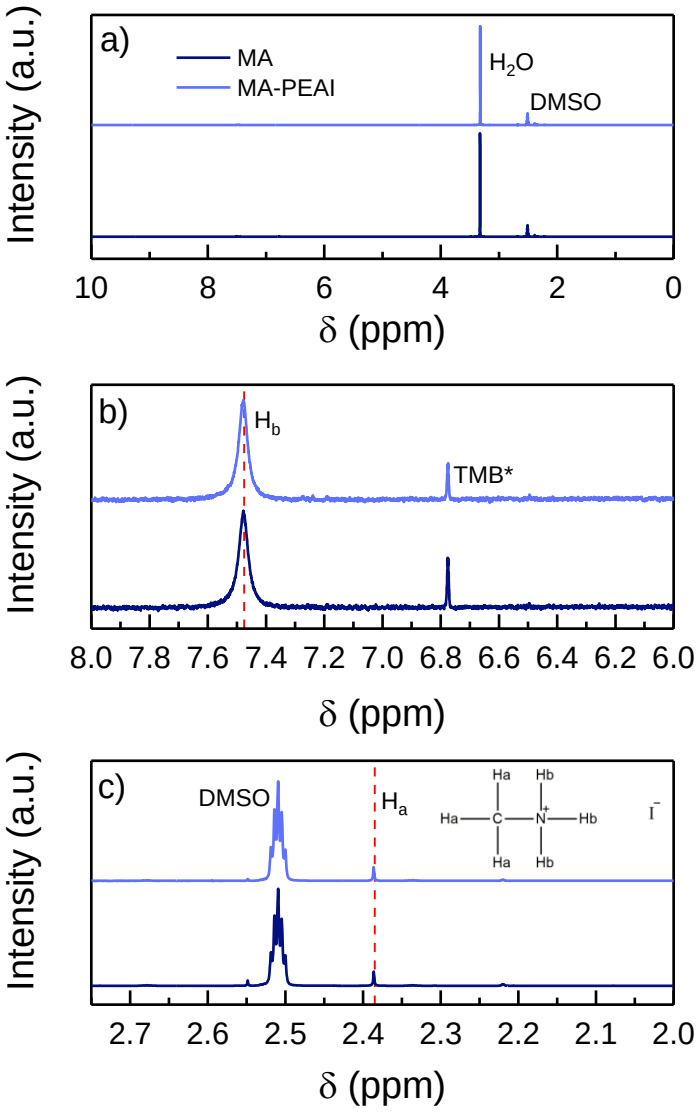

Figure S5. ^{1}H NMR spectra of $MAPbI_3$ perovskite and $MAPbI_3$ perovskite with PEAI as an additive in the antisolvent, with a concentration of 3 mg/mL. The films were prepared and dissolved in DMSO-d_6. a) The peaks at 2.51 and 3.35 ppm are proton peaks of DMSO and H_2O, respectively; b) The peaks of the NH_3 of the $MAPbI_3$ at 7.46 ppm and the 1,2,4-trimethylbenzene (TMB) used as internal standard; c) The peak of the -CH of the $MAPbI_3$ at 2.36 ppm; the peaks at 2.26 and 2.5 ppm correspond to CH_3- groups of the TMB and the sideband of the DMSO, respectively.

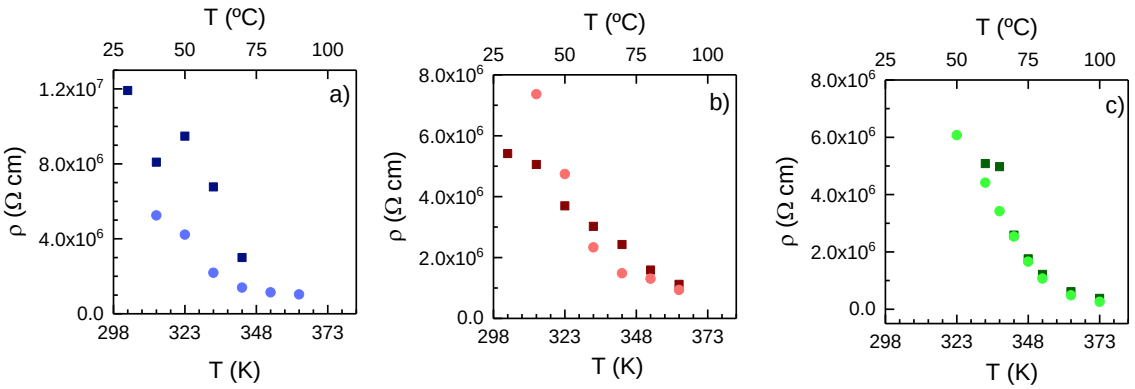

Figure S6. DC dark resistivity-temperature dependence for a) MA, b) $MA_{0.9}Cs_{0.1}$, and c) $MA_{0.5}FA_{0.5}$ thin films synthetized without (square) and with (circles) PEAI salt.

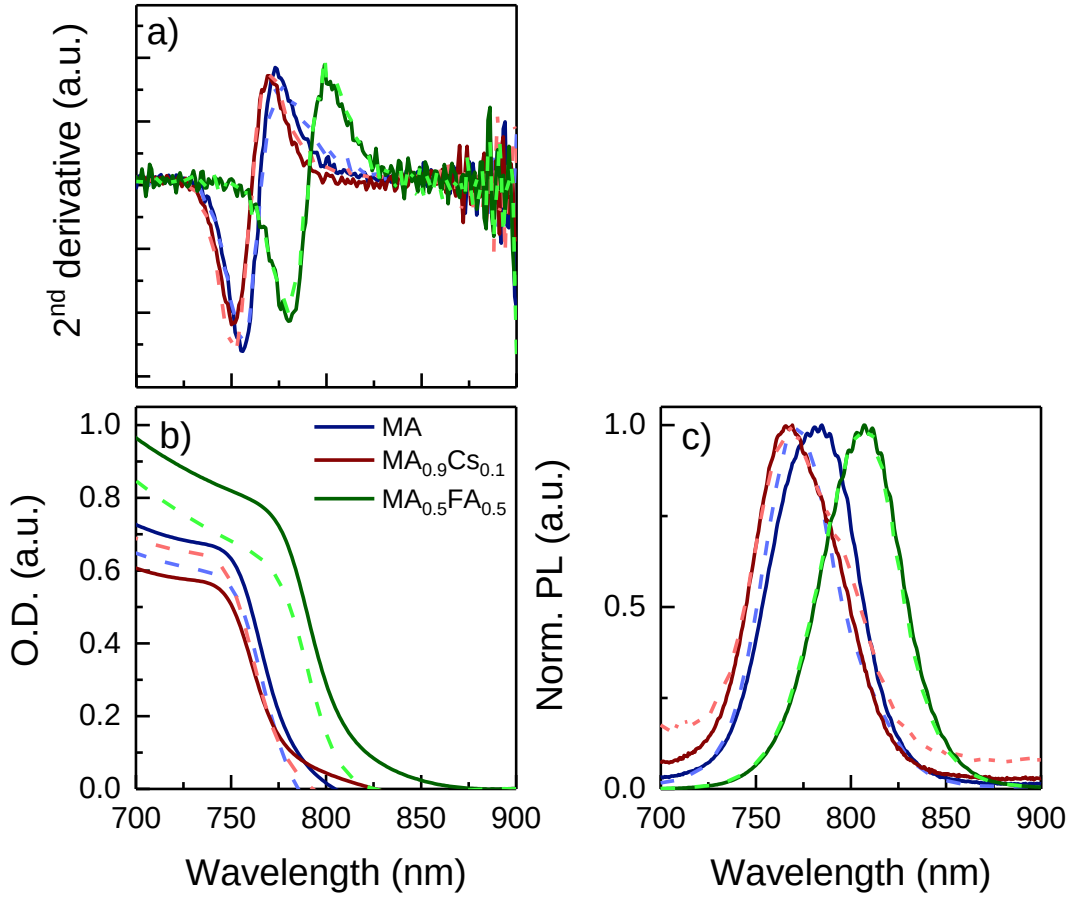

Figure S7. a) Second derivative of the optical density of the thin films and b) optical absorption. c) Normalized PL emission of the thin films. Solid and dashed lines correspond to samples without and with PEAI, respectively.

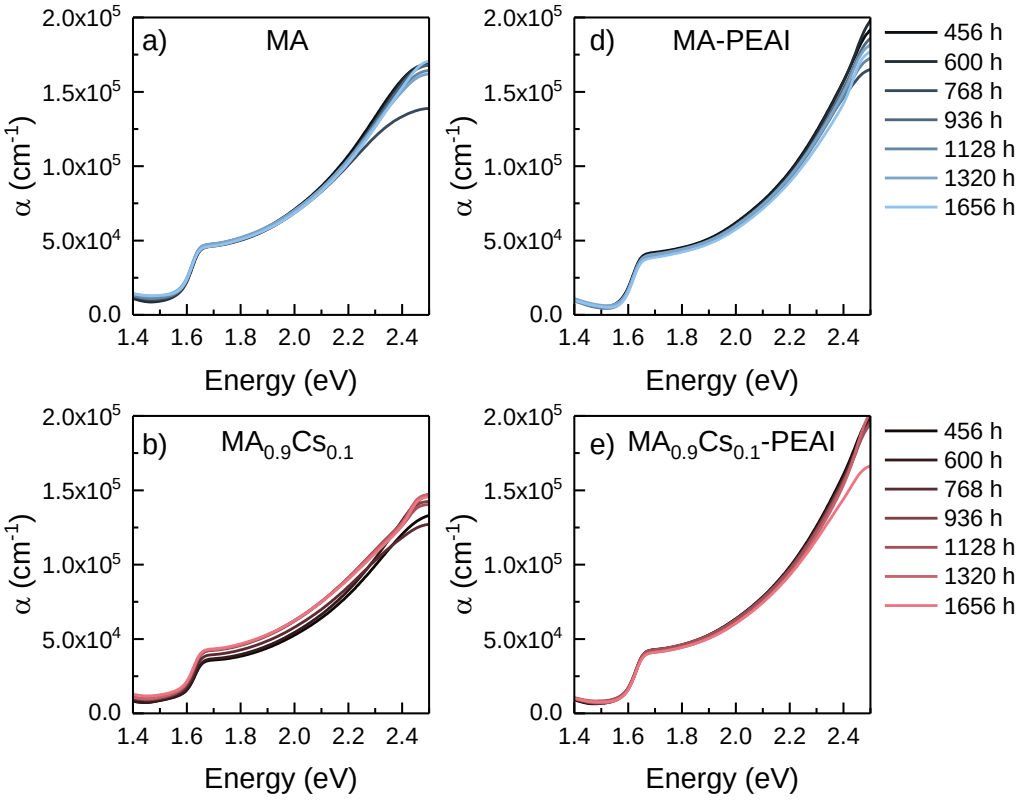

Figure S8. Absorption coefficient, α, over time of the perovskite films, MA, and $MA_{0.9}Cs_{0.1}$, w/o and w/PEAI in the antisolvent solution.

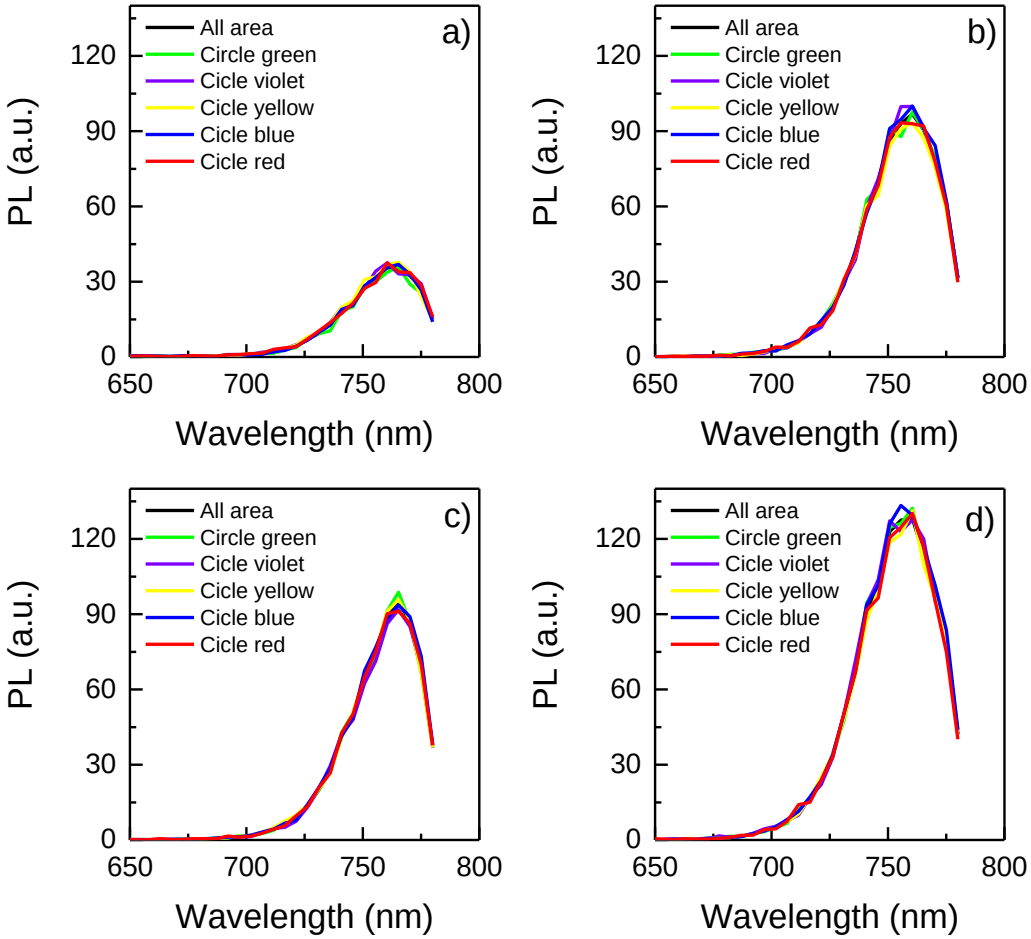

Figure S9. PL intensity spatial mapping for the perovskite films, a) MA, b) $MA_{0.9}Cs_{0.1}$, c) MA-PEAI, and d) $MA_{0.9}Cs_{0.1}$-PEAI. The area irradiated is depicted in Figure S10.

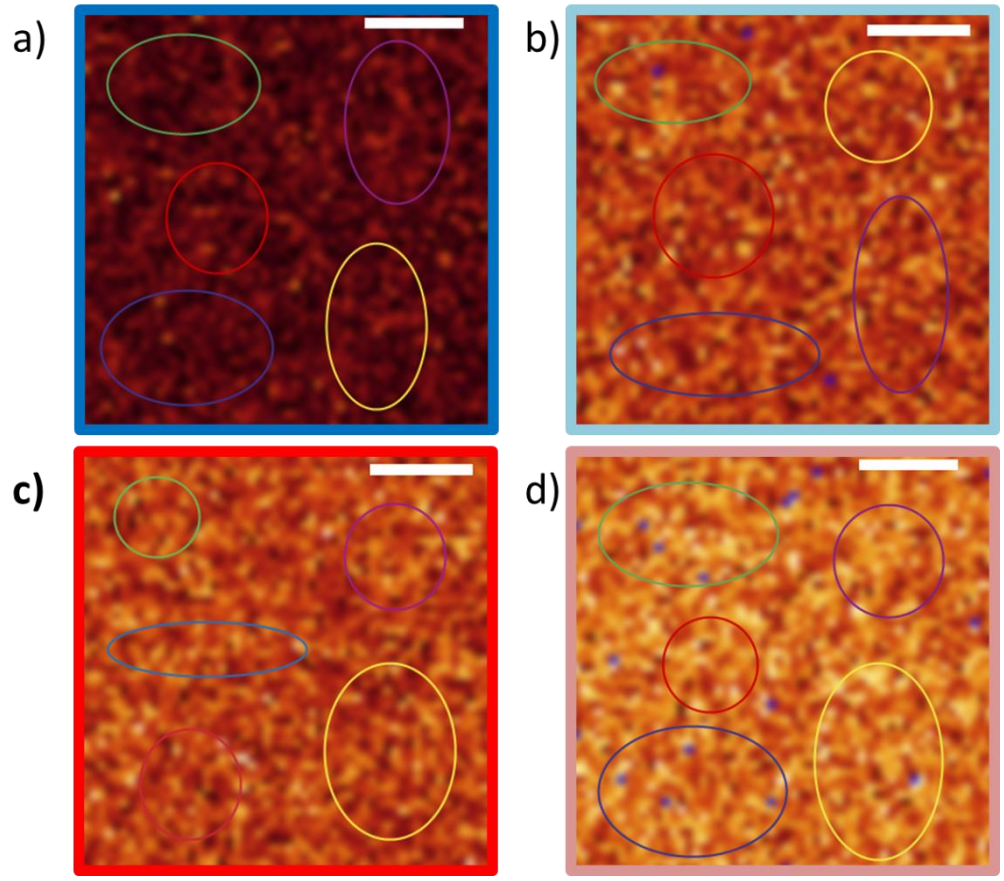

Figure S10. High-resolution PL confocal microscopy images mapping for the perovskite films, a) MA, b) $MA_{0.9}Cs_{0.1}$, c) MA-PEAI, and d) $MA_{0.9}Cs_{0.1}$-PEAI. The circles correspond to the area under study where bar scale corresponds to 5 μm length.

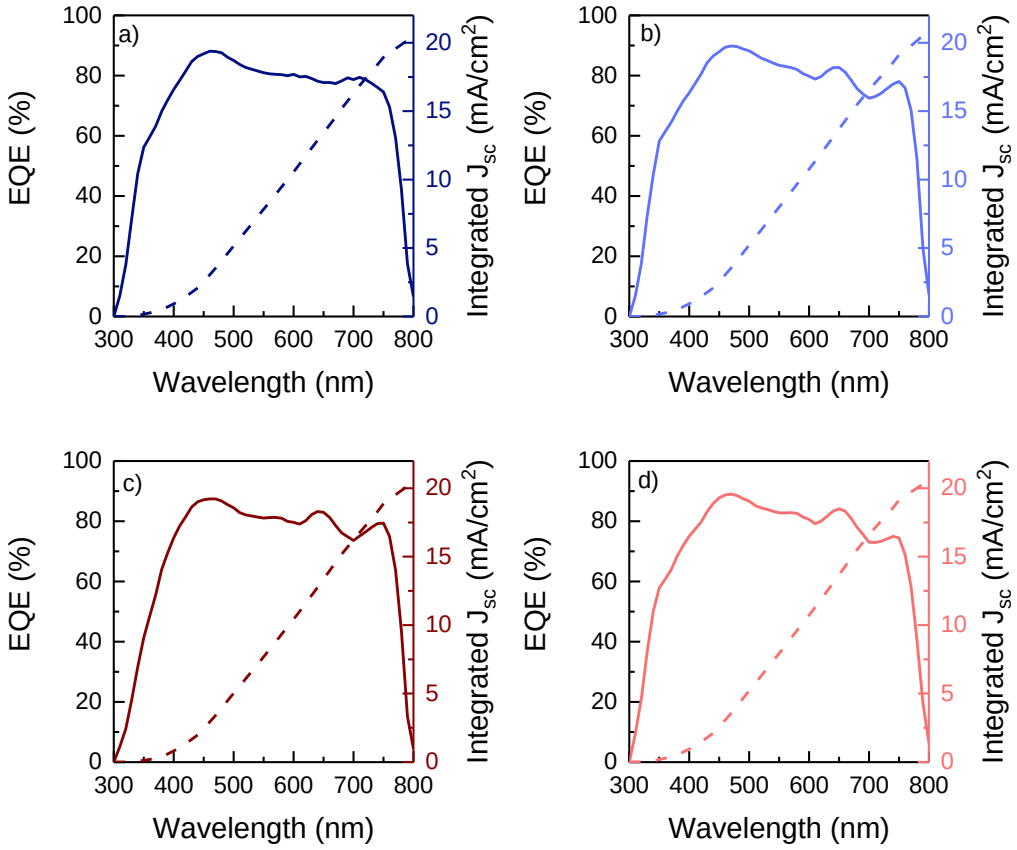

Figure S11. EQE and J_{sc} calculated by integration of EQE spectrum for a) $MAPbI_3$, b) $MAPbI_3$-PEAI, c) $MA_{0.9}Cs_{0.1}PbI_3$, d) $MA_{0.9}Cs_{0.1}PbI_3$-PEAI.

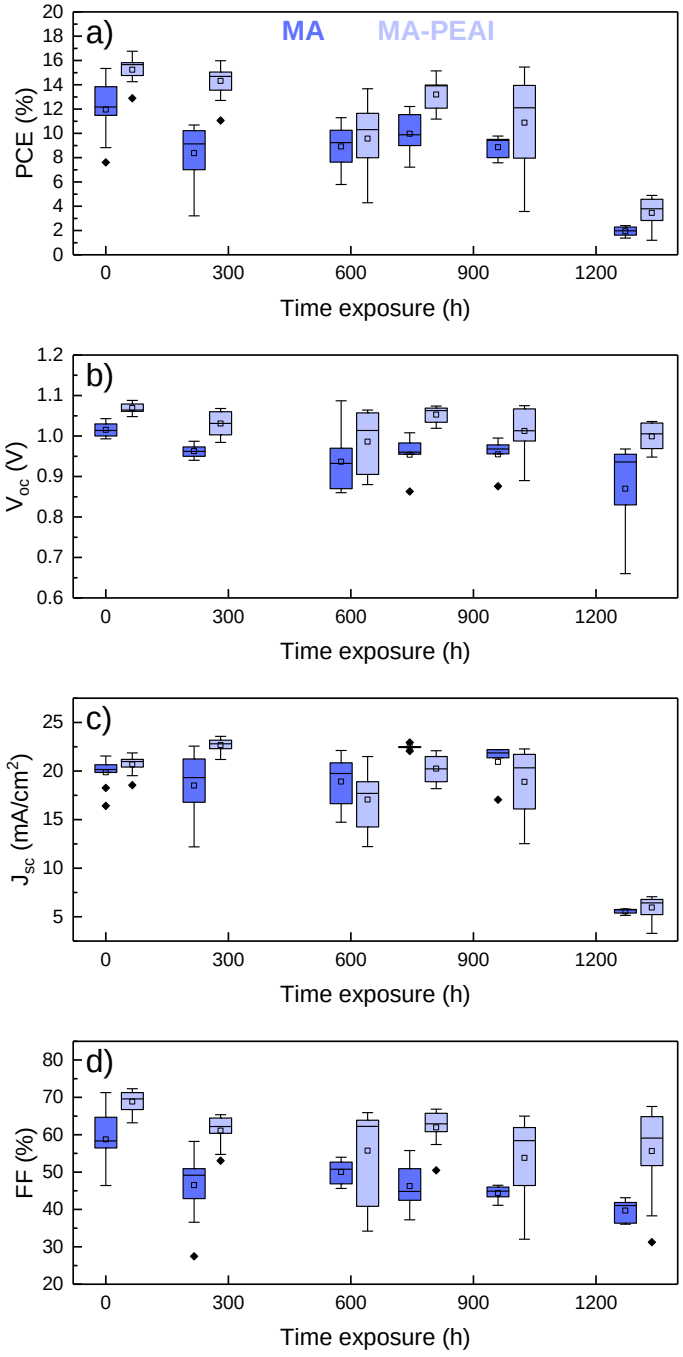

Figure S12. Photovoltaic parameters evolution for MA- (above) and MA-PEAI (below) PSCs over 1200 h. These data are extracted from J-V curves in forward direction under 1 sun illumination intensity.

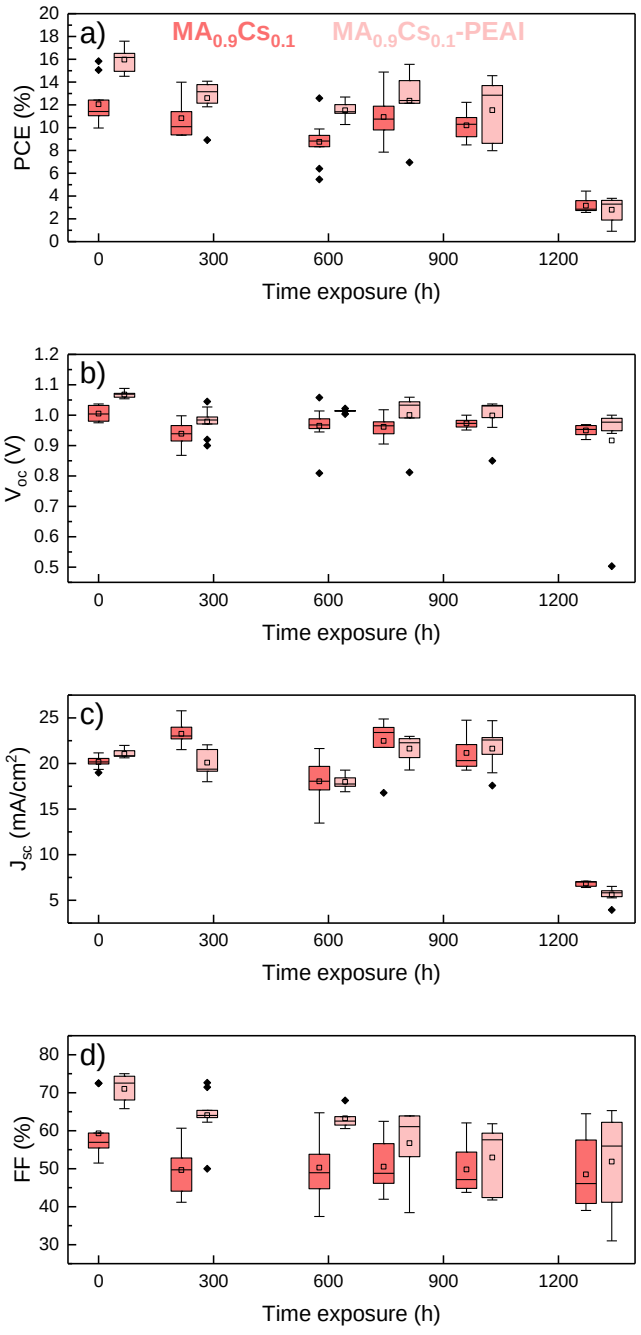

Figure S13. Photovoltaic parameters evolution for $MA_{0.9}Cs_{0.1}$- (above) and $MA_{0.9}Cs_{0.1}$-PEAI (below) PSCs over 1200 h. These data are extracted from J-V curves in forward direction under 1 sun illumination intensity.